Spatially resolved measurements of ballistic and total transmission in microscale tissue samples from 450 nm to 1624 nm

AARON T. MOK,[1,2,*] Ⓘ JAMIEN SHEA,[3] CHUNYAN WU,[1,4] Ⓘ FEI XIA,[1,2,5] Ⓘ ROSE TATARSKY,[3] NILAY YAPICI,[3] AND CHRIS XU[1]

[1] *School of Applied and Engineering Physics, Cornell University, NY 14853-3501, USA*
[2] *Meining School of Biomedical Engineering, Cornell University, NY 14853-3501, USA*
[3] *Department of Neurobiology and Behavior, Cornell University, NY 14853-3501, USA*
[4] *College of Veterinary Medicine, Cornell University, NY 14853-3501, USA*
[5] *Present address: Laboratoire Kastler Brossel, ENS-PSL Research University, CNRS, Sorbonne Université, Collège de France, Paris, France*
[*] *tm624@cornell.edu*

Abstract: We built a simple and versatile setup to measure tissue ballistic and total transmission with customizable wavelength range, spatial resolution, and sample sizes. We performed ballistic transmission and total transmission measurements of overlying structures from biological samples *ex vivo*. We obtained spatially resolved transmission maps to reveal transmission heterogeneity from five microscale tissue samples: *Danionella* skin, mouse skull bone, mosquito cuticle, wasp cuticle, and rat dura over a wide spectral range from 450 nm to 1624 nm at a spatial resolution of ~25 μm for ballistic transmission measurements and ~50 μm for total transmission measurements. We expect our method can be straightforwardly applied to measuring the transmission of other samples. The measurement results will be valuable for multiphoton microscopy. The total transmission of a sample is important for the collection of multiphoton excited fluorescence and the assessment of laser-induced sample heating. The ballistic transmission determines the excitation power at the focus and hence the fluorescence signal generation. Therefore, knowledge of ballistic transmission, total transmission, and transmission heterogeneity of overlying structures of animals and organs are essential to determine the optimal excitation wavelength and fluorophores for non-invasive multiphoton microscopy.

1. Introduction

Optical imaging with near-infrared (NIR) light [1–5] reduces light scattering in biological tissue. There is a need for quantitative measurements of tissue transmission in the NIR regime, particularly for the wavelengths range from 1200 nm to 1700 nm, where the best tissue penetration windows for high spatial resolution imaging lie. Multiphoton microscopy (MPM) uses NIR light for fluorophore excitation. For 2-photon excitation [6], wavelengths of ~800–1100 nm are typically needed. For 3-photon excitation [3], wavelengths of ~1200–1700 nm are needed. Non-invasive MPM of intact animals or organs [2,7] requires knowledge of optical transmissions of the overlying structures over a wide spectral range: ballistic transmission at the NIR excitation wavelength (~800 nm to ~1700 nm) determines the amount of excitation light at the focus and hence the multiphoton excited signal [4]; total transmission at the excitation wavelength governs sample heating [8,9]; total transmission in the visible range (~400 nm to ~700 nm) or at the fluorescence emission wavelengths affects fluorescence signal collection efficiency [10–12]. While optical properties for some tissues at NIR have been reported [13–16], optical transmission of a large number of biological samples, particularly at the long wavelengths (>1100 nm), are often not readily available [15,17].

The spatial heterogeneity of optical transmission in these structures is another essential factor that affects MPM imaging. For example, the presence of pigments on the sample will lead to high local absorption and impair imaging performance in some localized sample areas. However, current measurement methods for optical transmission using a double integrating sphere [3] or commercial UV-VIS-IR spectrophotometer [15] only provide tissue transmission averaged across ~mm to ~cm of the sample depending on the incident beam size. Microscale (μm - mm) overlying structures dissected from small species (e.g., *Danionella*, fruit flies, wasps, and mosquitoes) or localized pigments scattered across the structures are consequently challenging to measure.

Here we built a simple and versatile measurement setup (i.e., a tissue spectrometer) to measure the ballistic and total transmission of samples customizable for different wavelengths, spatial resolutions, and sample sizes. We measured the ballistic and total transmission with a photodetector coupled to a single-mode fiber (SMF) and an integrating sphere, respectively. We verified that the SMF effectively isolates ballistic photons by measuring tissue phantoms of known optical properties, and then comparing the results with theoretical predictions and measurements from a typical double-aperture setup [18]. We built a processing pipeline to calculate the transmission map of each sample and extract transmission data from different regions of interest (ROIs). We performed spatially resolved ballistic and total transmission measurements of overlying structures from microscale biological samples *ex vivo* and reported transmission maps to reveal transmission heterogeneity from five different tissue samples: *Danionella* skins, mouse skull bones, mosquito cuticles, wasp cuticles, and rat dura. Finally, we compared the results with previously reported *in vivo* and *ex vivo* data. Ballistic transmission is reported over a spectral range from 911 nm to 1624 nm, and total transmission is reported over a spectral range from 450 nm to 1624 nm. This measurement method can be straightforwardly applied to other biological samples. The results shown here will provide valuable guidance for high-resolution optical imaging such as MPM, where the ballistic transmission and total transmission are essential for determining the optimal excitation wavelength and fluorophores.

2. Experimental setup and methods

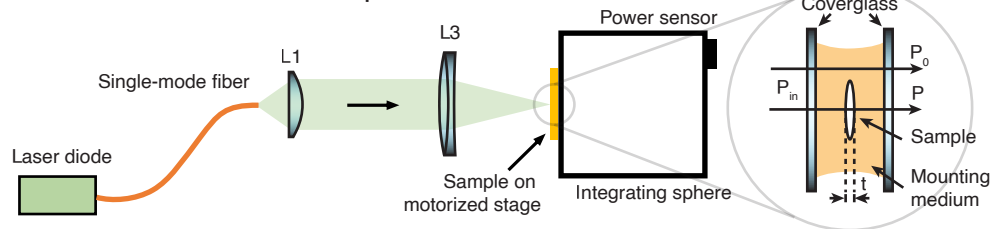### 2.1. Experimental setup and processing pipeline

Total transmission and ballistic transmission of the biological samples were measured using the setup shown in Fig. 1. Single-mode fiber-coupled laser diodes were used as the illumination sources, and the output light from the SMF was collimated using a lens (L1). For measurements of ballistic transmission (Fig. 1(A)), collimated light was focused with a lens (L2) to a spot size of ~25 μm ($1/e^2$ diameter) on the sample for all wavelengths. The Rayleigh range for a 25 μm focus spot is approximately 0.8–1.3 mm in water (refractive index ~ 1.33) for wavelengths between 911 nm and 1624 nm and longer than the thickness of all the samples measured in this paper (<0.6 mm). Therefore, the effects of the beam convergence/divergence and aberrations are negligible. The transmitted light through the sample was then demagnified using the same optics as the illumination side and coupled into another SMF connected to a power sensor (S142C or S146C, Thorlabs). For measurements of the total transmission (Fig. 1(B)), the collimated light was focused with a lens to a spot size of ~50 μm ($1/e^2$ diameter) on the sample for all wavelengths. The Rayleigh range for a 50 μm spot size is much larger than the sample thickness. An integrating sphere (S142C or S146C, Thorlabs) positioned right after the sample was used to detect the transmitted light. The sample was translated and raster-scanned with a motorized stage (MT3-Z8, Thorlabs) for ballistic transmission or total transmission measurement. At scanning step sizes of 25 μm and 100 μm, the imaging speed was, respectively, ~25 min/mm^2 and ~1.6 min/mm^2. The ballistic transmission of *Danionella* skin, Mosquito cuticle, wasp cuticle, and rat dura were scanned with a step size of 25 μm. The total transmissions of these four samples were scanned with a step size of 50 μm. The ballistic and total transmissions of the mouse skull

bone were scanned with a step size of 100 μm. Table 1 lists the laser diodes, the SMFs, and the lenses used at all wavelengths. The light from the SMFs at different wavelengths was collimated with different lenses (L1) to maintain approximately the same spot size on the sample at different wavelengths.
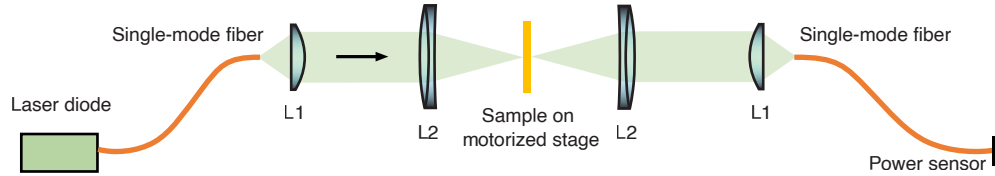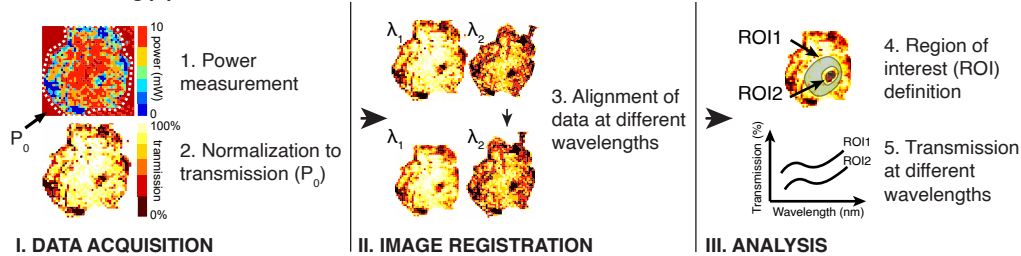

Fig. 1. Schematics of the transmission measurement setup and processing pipeline. (A) Setup for ballistic transmission measurements. (B) Setup for total transmission measurements. (Inset) Illustration of the power measurements through a mounted sample (C) Processing pipeline after transmission measurements. The location to obtain P_o is illustrated in the left panel in (C).

A custom script written in LabView 2019 (National Instruments) was used to control the motorized stage and record the transmission measurements at various spatial locations. For each sample, the first set of measurements at a wavelength was repeated after all measurements were taken to ensure that there was no sample dehydration or degradation throughout the measurement session. The repeated measurement results are within 0.5% of the first measurement results. A CMOS camera (DCC1545M, Thorlabs) or an InGaAs infrared camera (WiDy SWIR 640U-S, NIT) was set up in transmission mode to image the sample and the incident beam so that the incident light spot was close to the sample before scanning with the motorized stage.

Data acquired were spatially resolved power measurements inside and outside the sample, denoted as P and P_0, respectively (Fig. 1 inset). They were processed with a three-step pipeline (Fig. 1(C)) using a custom script written in Matlab (Matlab 2020b, Mathworks): first, P was normalized to P_0 (see 2.6 for more details), forming a transmission map; second, transmission maps measured at different wavelengths were aligned with image registration using similarity transformation; third, ROIs were segmented manually to extract transmission data of distinguishable features on the sample.

Table 1. Laser diodes, SMFs, and lenses used for different wavelengths.

λ (nm)	Laser diode	SMF	Lens		
			L1	L2	L3
450	LP450-SF15, Thorlabs		F671-APC-405	N/A	AC254-045-A
514	LP520-SF15, Thorlabs	P3-488PM-FC-2	F240-APC-532	N/A	AC254-100-A
630	LP633-SF15, Thorlabs				
911	LP915-SF15, Thorlabs	P3-780PM-FC-2	F220-APC-980	AC254-50-B	AC254-100-B
1056	DFB-1054-PM-50, Immulume				
1300	FPL1053P, Thorlabs				
1487	FOL1404QQM, FITEL	P3-1310PM-FC-5	F280-APC-1550	AC254-50-C	AC254-100-C
1552	ILX FOS-79800D, Lightwave				
1624	FPL1059P, Thorlabs				

2.2. Wavelength selection and validation of the transmission measurements

Nine continuous-wave (CW) lasers (Table 1) centered at nine wavelengths used in this study are measured with a spectrometer (OSA205C, Thorlabs) (Fig. 2(A)). Ballistic transmissions were measured at six different wavelengths (911 nm, 1056 nm, 1300 nm, 1487 nm, 1552 nm,1624 nm), covering the spectral range for typical 2-photon and 3-photon excitation. The total transmission was measured at nine different wavelengths (450 nm, 514 nm, 630 nm, 911 nm, 1056 nm, 1300 nm, 1487 nm, 1552 nm, and 1624 nm). It covers the typical 2-photon and 3-photon excitation spectral range and includes the typical emission wavelengths of blue, green, and red fluorophores for MPM.

Total transmissions obtained by the tissue spectrometer at four wavelengths (1300 nm, 1487 nm, 1552 nm, 1624 nm) were compared with previously reported results for water [16]. 1-mm-thick deionized water (BT121925-4L, VWR) was used (Fig. 2(B)).

Ballistic transmission measurement results from the tissue spectrometer were compared at five wavelengths (911 nm, 1056nm, 1300 nm, 1552 nm, 1624 nm) to both calculated values using Mie scattering and measurement results from a double-aperture setup (Fig. 2(C)). Mie function developed in Matlab [19] was used to simulate the ballistic transmission of the tissue phantoms. The double-aperture setup used the beam collimated by L1 and followed by four 2 mm apertures in separations of 100mm, 90mm, and 100mm. The aperture separations provided an acceptance half-angle of 0.395°. The sample was placed between the second and the third aperture. A power meter (S132C, Thorlabs) was placed immediately after the fourth aperture. Four tissue phantoms were used for the comparisons: two 1-mm-thick phantoms with 2-μm-diameter polystyrene beads at a concentration of 2.95×10^8 beads/ml (0.12% volume fraction) and 6.05×10^8 beads/ml (0.25% volume fraction) in 2% agarose; and two 200-μm-thick phantoms with the same beads and concentrations in 2% agarose. The anisotropy factor (g) for 2-μm-diameter polystyrene beads was calculated to be 0.92 at 900 nm and 0.89 at 1,700 nm, similar to many biological samples [20]. Measured transmission values obtained by the double-aperture setup (error bar in green) and the tissue spectrometer (error bar in purple) were normalized to 2% agarose (without the beads) of the same thickness. The error bar indicates the standard deviation of the measurement.

We further compared the retrieved numbers of scattering lengths to the expected numbers of scattering lengths predicted by Mie theory (Fig. 2(D)). It showed that the accuracy of the tissue spectrometer (black dot) is within 6.5% of the expected value up to 7 scattering lengths. We further performed simulations with OpticStudio (Zemax OpticStudio 20.3.2) to examine the contribution from non-ballistic photons when using a double-aperture setup at an acceptance
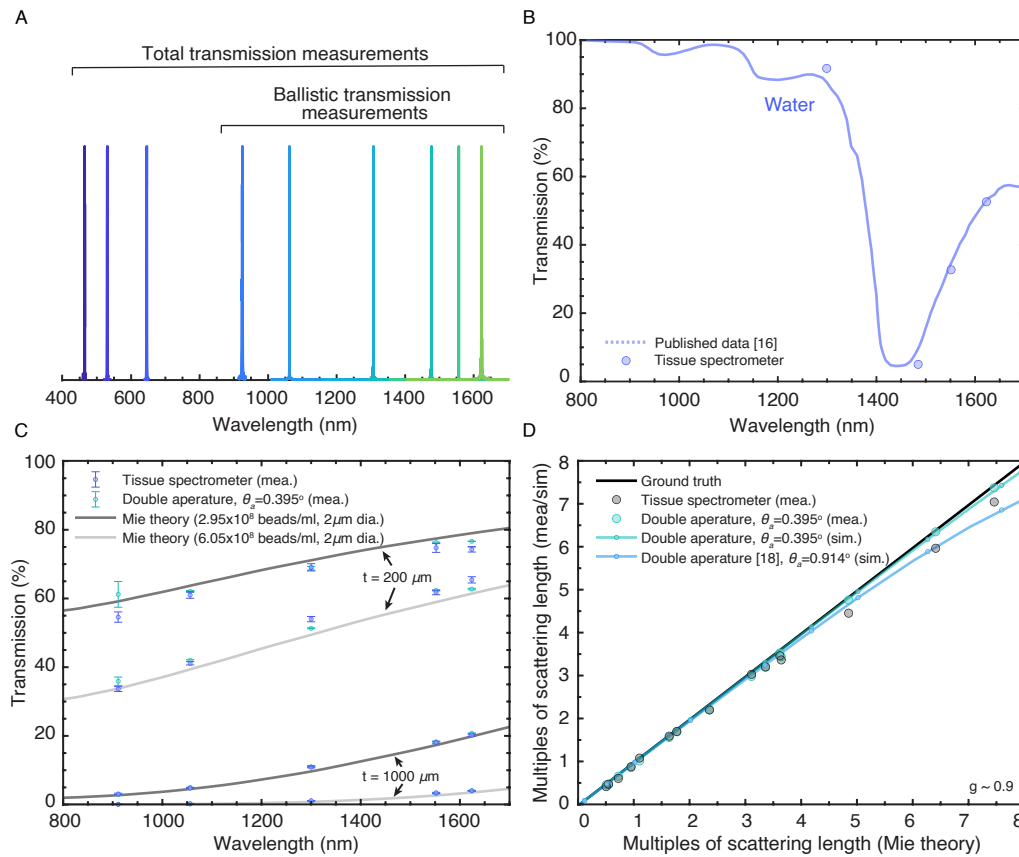
Fig. 2. Wavelength selection and validation of the tissue spectrometer accuracy. (A) Wavelength measurements of the CW lasers used. (B) Total transmission of water measured by the tissue spectrometer (circle dot) compared to previous measurements [16]. (C) Ballistic transmission of four tissue phantoms measured by the tissue spectrometer (purple error bar) and compared to the Mie theory (solid line) and measurements using a double-aperture setup at 0.395° acceptance angle (green error bar). (D) Comparison of the retrieved multiples of scattering length to the predicted multiples of scattering length. Mea. = measurement, sim. = simulation.

half-angle of 0.395° (green line) and a published double-aperture setup [18] at 0.914° (blue line). The simulation was done in non-sequential mode at a wavelength of 1320 nm in OpticStudio. The tissue sample was modeled as a rectangular volume at a thickness of 0.5 mm with no absorption. The sample size was 4 mm x 4 mm. The refractive index was 1, and photons scattered to the boundary of the sample were not absorbed. The scattering mean free path (MFP) of the sample was varied. The anisotropy factor was 0.9. For each condition, five simulations were run, each with 10 million photons. The mean values from the simulation at different conditions are shown in dots and fitted lines (green and blue). The standard deviation of all simulations is <0.009 multiples of the MFP. The simulated double-aperture setup with an acceptance half-angle of 0.395° is consistent with the experimental results.

Results in Fig. 2(D) showed that the measurement values obtained by the tissue spectrometer agree closely with those predicted by Mie theory and the double-aperture setup at 0.395° acceptance half-angle: <3.5% difference up to 3.5 scattering length and <6.5% difference up to 7 scattering lengths.

2.3. Sample preparation

All animal experiments and housing procedures were conducted following Cornell University Institutional Animal Care and Use Committee guidance. Samples were extracted and mounted differently to preserve them for transmission measurements that may span many hours. All surgical procedures were done on the same day of the measurements.

Danionella skin (6-months to 1-year-old*, female, Danionella dracula*) was extracted from the region of skin containing pigmentation over the entire brain with fine forceps and microscissors. During the surgery, the *Danionella* was euthanized in benzocaine solution and was completely submerged in phosphate-buffered saline (PBS). The dissected skin was moved in PBS using a transfer pipette onto a #1.5 coverslip with silicone gel as a spacer along the edges. Any air bubbles were removed. The skin sample was laid flat, and any folding was removed with fine forceps. A second #1.5 coverslip was placed on the top to make a buffer-filled chamber for the sample.

Mouse (15–16 weeks old, male, C57BL/6J, The Jackson Laboratory) skull bone extraction was performed using the procedure described in [21]. In brief, a piece of 4 to 5 mm diameter skull bone was extracted at ~2.5 mm lateral and ~2 mm caudal from the bregma point over the somatosensory cortex with a dental drill. The bone was kept hydrated with PBS at all times during the surgery and before being mounted. The extracted skull was immersed in 2% agarose and mounted between two #1.5 coverslips separated with a 0.15-mm spacer (70327-13S, EMS). Skull bones thicker than 0.15 mm were accommodated with agarose on the top of the spacers.

Mosquito (2 to 3 weeks post eclosion, female, *Aedes aegypti*) and wasps (male, *Polistes dominula*) cuticles were isolated from the medial portion of the dorsal head after being deeply anesthetized on ice for 5 minutes. The eyes, proboscis, brain, and other soft tissues were cleaned from inside the cuticle with a razor blade. Any air bubbles were removed from the cuticle. The cuticle samples were laid flat, and any folding was removed with fine forceps. The extracted cuticles were sandwiched between two #1.5 coverslips with Bondic UV curable resin (part # SK8024).

Rat (24 to 27 weeks old, male, Sprague Dawley, Charles River Laboratories) dura extraction was performed using a similar procedure described in [22]: skull bone between bregma and lambda was thinned with a dental drill and removed. Dura was then cut with a syringe and lifted with a pair of forceps. The extracted dura was cleaned and laid flat with Q-tips and gelfoam sponges in PBS. The extracted dura was sandwiched between two #1.5 coverslips with Bondic UV curable resin (part # SK8024).

2.4. Sample thickness measurements

The thickness of the mouse skull bone was measured by a ball micrometer. The thickness of other samples was measured by taking a z-stack using third-harmonic generation (THG) microscopy with a water immersion objective lens (25x, 1.05NA, XLPLN25XWMP2, Olympus). THG has a strong signal at the interface between the mounting medium and the sample, therefore allowing thickness measurement of the sample [23].

2.5. Sample transmission correction

Measured sample transmission (P/P_o) was adjusted to account for the difference in transmission of mounting mediums (i.e., water, 2% agarose, and UV curable resin) at each wavelength. Since light passed through the surrounding mounting medium encounters absorption but negligible scattering (Fig. 1 inset), the reported transmission ($T(\lambda)$) for each sample is corrected using Eq. (1). It accounts for the absorption of the mounting medium with the thickness of the sample.

$$T(\lambda) = \frac{P(\lambda)}{P_o(\lambda)} \cdot e^{-\mu_m(\lambda)t} \tag{1}$$

where $T(\lambda)$ is the reported transmission at wavelength λ, $P_0(\lambda)$ is the measured power of the beam that passes through the surrounding mounting medium, $P(\lambda)$ is the measured power of the beam that passes through the sample, $\mu_m(\lambda)$ is the absorption coefficient of the mounting medium, and t is the thickness of the sample. $\mu_m(\lambda)$ of water and 2% agarose are assumed to be the same and obtained from previous measurements [16]. The absorption coefficient of the UV curable resin is measured with a spectrophotometer (Cary 5000 UV-Vis-NIR, Agilent). The transmission of the resin is shown in Fig. S1. The accuracy of $\mu_m(\lambda)$ obviously affects the accuracy of the reported transmission. However, $\mu_m(\lambda)$ is well-established for water, and for the UV curable resin, $\mu_m(\lambda)$ has negligible impact on the measurements due to the small thickness of the sample ($<100\,\mu$m) (See Fig. S1).

3. Results

Wide-field transmission images obtained by cameras, spatially resolved ballistic transmission, and spatially resolved total transmission at selected wavelengths were shown in Fig. 3. Pigments and distinguishable spatial structures, such as the ommatidia of the compound eye on the mosquito cuticle and the holes for ocelli on the wasp head, were indicated.
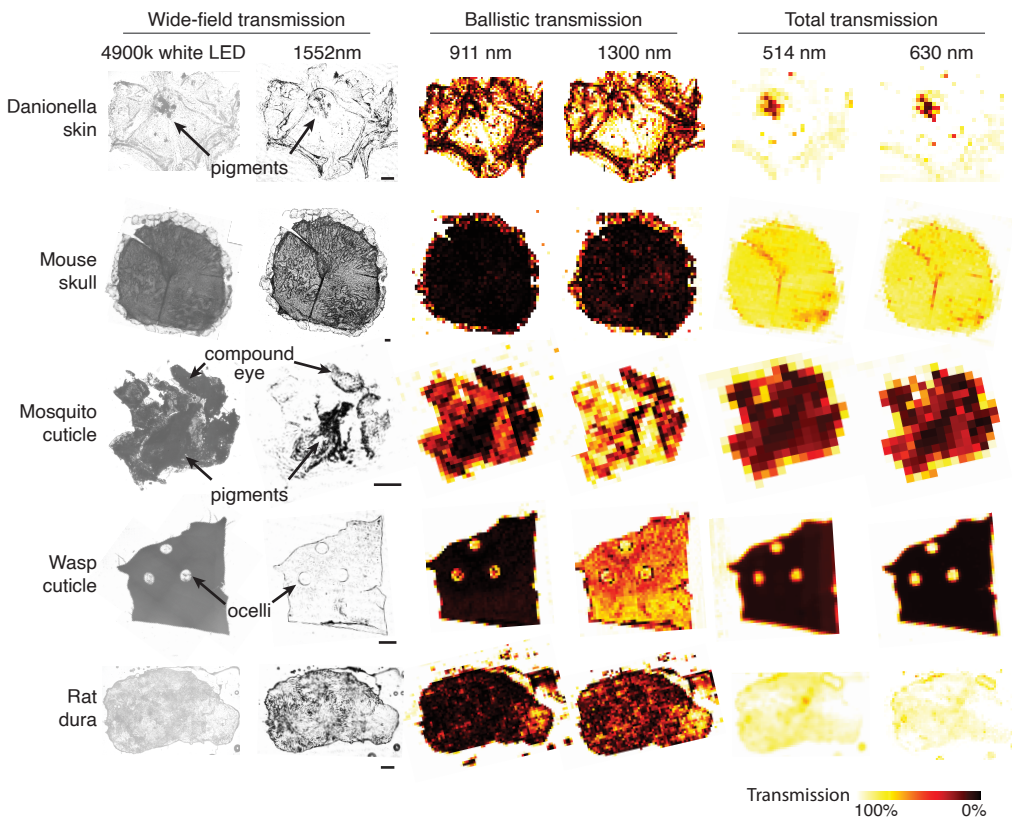

Fig. 3. Spatially resolved transmittance map of samples obtained by wide-field, ballistic, and total transmission measurements at selected wavelengths. Wide-field transmission images using 4900k white LED and 1552 nm, ballistic transmission at 911 nm and 1300 nm, and total transmission at 514 nm and 630 nm of *Danionella* skin, mouse skull, mosquito cuticle, wasps cuticle, and rat dura are shown. Scale bar = 200 μm. The colors represent transmission from 0% to 100% at different spatial locations on the samples.

Ballistic transmission data were shown as violin plots and box plots to show the distribution of the transmission data (Fig. 4). The violin plots showed the distribution of measurements for all spatial locations. The box plots showed the median, lower quartile, upper quartile, minimum, and maximum of all spatial locations without outliers larger than the 1.5 interquartile range. *Danionella* skins and mosquito cuticles data were separated into pigmented and non-pigmented areas; wasps cuticles were separated into area caudal and rostral to the ocelli. Total transmission data were also shown with violin plots and box plots (Fig. 4) with the same visualization schemes as the ballistic transmission.
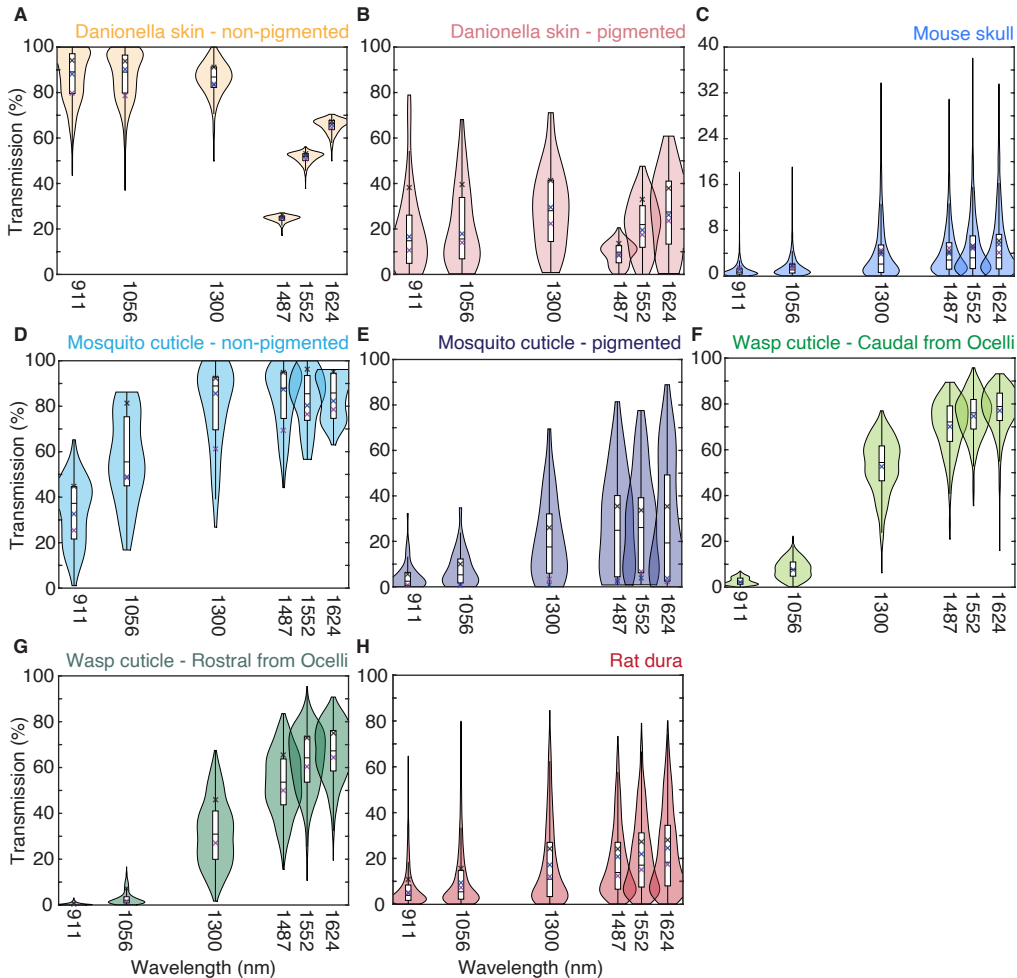

Fig. 4. Ballistic transmission of (A) non-pigmented *Danionella* skins, (B) pigmented *Danionella* skins, (C) mouse skulls, (D) non-pigmented mosquito cuticles, (E) pigmented mosquito cuticles, (F) wasp cuticles at region caudal from the ocelli, (G) wasp cuticles at region rostral from the ocelli, and (H) rat dura. Violin plots showed the distribution, and box plots showed the median, lower quartile, upper quartile, minimum, and maximum of measurements for all spatial locations. The crosses showed the transmission mean of each animal sample. See Dataset 1 [24] for underlying values.

The thickness of the *Danionella* skins, mosquito cuticles, wasp cuticles, and rat dura was measured with THG as ~580 μm, 100 μm, 90 μm, 65 μm, respectively (see section 3.4). The sample thickness reported here is the axial movement of the objective lens. Hence, the actual

thickness may be slightly underestimated due to the refractive index difference between the objective immersion medium (i.e., water) and the sample. The thickness of the mouse skulls (∼170 μm) was measured with a ball micrometer.

The mean ballistic transmission and total transmission of all the data points from different animals were tabulated in Table 2 and Table 3, respectively. Samples from three individual animals were measured (N = 3), and the number of spatially resolved data points acquired was also indicated (n). The animal-to-animal variation is minimal. It is indicated in the violin plots (Fig. 4 and 5), showing unimodality for most distributions. The mean of transmission from each animal was indicated as crosses in the plot. Transmission through distinguishable ROIs in the samples was shown separately to account for the differences in optical transmission. "Non-pigment" showed the transmission of the non-pigmented areas, while "pigment" showed the transmission of pigmented areas. "Cau" and "Ros" showed the transmission of areas caudal and rostral from ocelli, respectively.

Table 2. Mean and standard deviation (SD) of ballistic transmissions of different samples

	Danionella skin		Mouse skull	Mosquito cuticle		Wasps cuticle		Rat dura
	Non-pigment	Pigment		Non-pigment	Pigment	Cau	Ros	
N	3		3	3		3		3
n	491	69	2152	61	60	614	1031	2912
Mean (SD.) ballistic transmission (%)								
911 nm	87.2 (11.2)	19.0 (18.4)	1.0 (1.2)	33.7 (13.9)	4.5 (5.9)	2.7 (1.6)	0.5 (0.5)	7.0 (8.9)
1056 nm	87.3 (10.5)	21.2 (17.5)	1.6 (1.8)	57.3 (19.0)	7.9 (8.0)	8.2 (4.2)	3.0 (3.0)	10.8 (12.7)
1300 nm	86.1 (7.4)	29.0 (17.3)	4.0 (4.9)	80.1 (18.1)	20.4 (17.6)	53.5 (11.8)	31.4 (14.2)	17.7 (18.3)
1487 nm	24.8 (1.5)	9.4 (4.9)	4.2 (4.3)	84.0 (13.4)	27.6 (21.8)	71.0 (11.7)	53.6 (13.9)	18.7 (15.6)
1552 nm	51.5 (2.4)	21.6 (11.7)	4.9 (5.1)	83.4 (12.1)	27.0 (21.7)	75.6 (9.7)	63.3 (13.3)	21.1 (16.5)
1624 nm	65.5 (3.2)	27.6 (17.0)	5.3 (5.5)	84.5 (9.5)	27.5 (26.1)	78.0 (10.0)	66.9 (12.3)	23.0 (17.9)

Table 3. Mean and standard deviation of total transmissions of different samples

	Danionella skin		Mouse skull	Mosquito cuticle		Wasps cuticle		Rat dura
	Non-pigment	Pigment		Non-pigment	Pigment	Cau	Ros	
N	3		3	3		3		3
n	190	27	1156	25	18	481	1557	2602
Mean (SD.) total transmission (%)								
449 nm	-	-	69.1 (6.8)	8.5 (3.0)	9.1 (8.0)	2.0 (0.3)	1.6 (0.5)	79.1 (8.0)
514 nm	97.1 (5.1)	43.3 (20.4)	76.1 (4.7)	18.0 (4.4)	15.6 (5.5)	5.5 (2.5)	5.2 (1.6)	86.2 (6.0)
630 nm	98.2 (4.9)	50.6 (21.4)	78.2 (3.9)	22.1 (8.9)	13.4 (18.7)	1.9 (0.2)	1.6 (0.2)	90.2 (5.5)
911 nm	98.3 (3.3)	67.6 (15.9)	86.8 (3.8)	68.3 (4.1)	42.1 (13.2)	11.3 (2.3)	7.6 (2.4)	94.6 (3.9)
1056 nm	98.9 (1.2)	79.6 (8.9)	90.5 (3.1)	84.4 (4.4)	59.0 (13.0)	34.0 (4.4)	23.1 (6.2)	95.0 (2.3)
1300 nm	92.8 (1.0)	84.0 (4.0)	88.9 (2.1)	92.1 (5.0)	69.5 (15.6)	74.4 (3.1)	59.8 (6.0)	97.6 (2.1)
1485 nm	26.2 (0.3)	24.6 (1.1)	76.9 (2.9)	94.3 (3.7)	71.5 (14.8)	85.1 (2.0)	72.8 (5.9)	87.8 (4.3)
1552 nm	54.2 (0.6)	51.2 (1.8)	81.5 (3.1)	94.7 (3.7)	71.7 (14.0)	88.2 (2.6)	78.1 (5.6)	93.2 (2.2)
1624 nm	68.8 (0.9)	65.6 (1.7)	85.3 (2.0)	95.6 (5.5)	77.4 (19.5)	91.0 (1.7)	80.9 (5.8)	94.1 (2.4)

We further compare the *ex-vivo* measurements in this study to the *in-vivo* and *ex-vivo* measurements reported in a previous study in the case of mouse skull. In this study, the mean and standard deviation of the mouse skull effective attenuation length (EAL) at 1300 nm and 1624
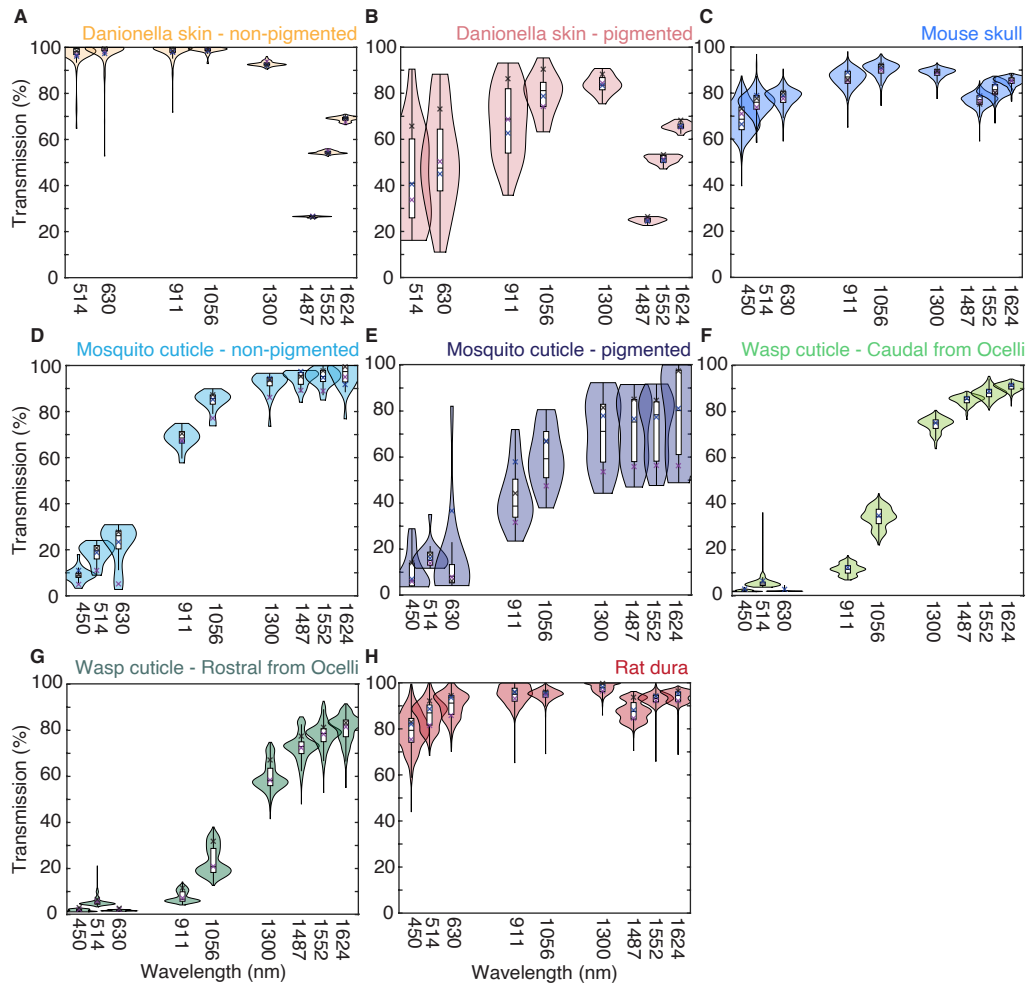
Fig. 5. Total transmission of (A) non-pigmented *Danionella* skins, (B) pigmented *Danionella* skins, (C) mouse skulls, (D) non-pigmented mosquito cuticles, (E) pigmented mosquito cuticles, (F) wasp cuticles at region caudal from the ocelli, (G) wasp cuticles at region rostral from the ocelli, and (H) rat dura. Violin plots showed the distribution, and box plots showed the median, lower quartile, upper quartile, minimum, and maximum of measurements for all spatial locations. The crosses showed the transmission mean of each animal sample. See Dataset 2 [25] for underlying values.

nm is 52.8 ± 20.1 μm and 57.9 ± 20.4 μm, respectively, by using the mean value of the ballistic transmission (I_b) in Table 2 and assuming sample thickness (t) is uniform across the sample (i.e., $EAL = -\frac{t}{ln(I_b)}$). Wang *et al.* [7] measured the EAL of the skull bone *in vivo* to be ~60 μm at 1320 nm and ~70 μm at 1700 nm using THG imaging of the skull. One possible explanation of the differences is the reduced surface scattering or aberration in the *in-vivo* experiments. An ultraviolet-curable glue was applied to the outer surface of the skull in the *in-vivo* experiments. The refractive index of the glue is higher than water and approximately matches the index of the skull bone. Therefore, the glue reduces scattering and aberration at the interface between the bone and the immersion medium. In addition, *ex-vivo* experiments measured the light exiting the skull, which encounters another interface between the bone and agarose with associated scattering and aberration. Nonetheless, considering the possible variations between individual mice and the large differences of the scattering lengths at various spatial locations, represented by the standard deviations of our measurements, the *ex-vivo* and *in-vivo* results are in reasonable agreement (<20% difference). Our results are also close (within ~ 10%) to that reported for pig skull bone and human cranial bone [26,27].

4. Discussion

Ballistic transmission measures the combined effects of tissue scattering and absorption. Both cause the ballistic photons to decrease exponentially as the propagation distance, with a characteristic length defined by the EAL [3,4]. Achieving diffraction-limited spatial resolution deep within scattering tissues generally requires imaging with ballistic photons. Ballistic transmission is perhaps the most important parameter in imaging modalities such as one-photon confocal, 2-photon, and 3-photon imaging. Our results showed that the long-wavelength windows of 1300 nm and 1700 nm are favored to achieve the best ballistic transmission. Although absorption by a sample is also dependent on its scattering property, total transmissions provide good estimations of the absorption of the samples measured. Total transmission through the sample is relevant for collecting multiphoton excited fluorescence and essential for assessing laser-induced sample heating. For all samples measured in this work, including the pigmented areas, total transmissions are generally high (~ 60% or higher) at 1300 nm and 1624 nm. These results indicate that heating in these samples, which is comparable to that in many long wavelength MPM applications [3], is likely manageable at the long-wavelength windows for deep tissue imaging. The total transmission of the non-pigmented areas of *Danionella* skin is similar to pure water (< 3% lower than pure water), and the small differences between the total transmission and the ballistic transmission show that scattering is negligible. The pigmented areas of *Danionella* skin show much stronger scattering, which appears to decrease as the wavelength increases.

The ballistic transmission measurement setup uses an SMF as the illumination source and detection device to isolate ballistic photons. This single-mode to single-mode coupling is an effective way to isolate ballistic photons. Any scattering events between the illumination and detection would scatter the light from its original mode into another mode [28]. Since transmission of light other than the fundamental mode is prohibited in the SMF, scattered light will not be detected. In order words, scattered light cannot be coupled into a SMF. We have experimentally verified that even after a large number of scattering events (>7), the measured number of scattering events is in good agreement with the expected number. This means that the detected photons are truly ballistic using our SMF approach.

The measurements were performed at discrete wavelengths that covered the spectral range of interest in MPM. It is straightforward to include additional wavelengths if desired. In addition, wavelength-tunable lasers or a supercontinuum source can also be used to provide continuous coverage over a specific spectral range, albeit at a high additional cost. Since tissue absorption and scattering typically do not show sharp spectral features in the visible and NIR spectral range, a set of low-cost CW laser diodes with wavelength spacing of 50 to 100 nm will likely provide

sufficient spectral coverage for biological imaging purposes. In the case of 2- and 3-photon fluorescence imaging, the considerable spectral width of the femtosecond pulsed lasers and the broad excitation and emission spectra of typical fluorophores provide additional practical reasons for using a discrete set of wavelengths.

This study measured spatially resolved ballistic and total transmission of samples at different wavelengths. These measurements provided the quantitative information necessary for MPM. In fact, the measurements presented in our paper is more valuable for MPM than the optical properties of the tissues since one must convert the optical properties to the total and ballistic transmissions to assess the performance of MPM at various wavelength. While animal-to-animal variations exist in total and ballistic transmissions, similar variations also exist in optical properties even when the animal species and age are specified. The measurement presented here can immediately predict the expected photons at the focus after passing through the tissue, the laser-induced sample heating, and the fluorescence collection efficiency in MPM. Combined with spatially resolved transmission measurement, these measurements guide the selection of excitation wavelength, fluorophores and enable a better understanding of the imaging performance.

MPM needs a high ballistic transmission at the NIR wavelengths and high total transmission at the visible wavelengths. Since mouse skulls have 4 to 5 times higher ballistic transmission at wavelength >1300 nm than at wavelength <1000 nm and similar total transmission across the spectrum (450 nm– 1634 nm), long-wavelength 2- or 3-photon microscopy must be used for transcranial mouse brain imaging. Furthermore, the superior confinement of 3-photon excitation will increase the penetration depth through the intact skull [7]. The increased ballistic transmission at longer wavelengths with similar total transmission across the spectrum implies reduced scattering at longer wavelengths for the mouse skull. An appropriate dye with NIR excitation and NIR emission can also enable one-photon transcranial imaging with improved contrast [2]. On the other hand, the wasp and mosquito cuticles have high ballistic transmission for wavelengths >1300 nm but low total transmission at the visible wavelength. Therefore, long-wavelength confocal microscopy [5] that utilizes NIR dye may be preferable for transcuticle imaging in these insects.

5. Conclusion

Knowledge of the optical transmission from the overlying structures of samples is an essential parameter when performing MPM. We built a versatile tissue spectrometer that can be straight-forwardly applied to measure spatially resolved ballistic and total transmission of biological specimens in a customizable setup for different wavelengths, spatial resolutions, and sample sizes. We measured ballistic transmission and total transmission of overlying structures from biological samples in microscale *ex-vivo*. We reported the ballistic and total transmission map to reveal transmission heterogeneity from five tissue samples: *Danionella* skin, mouse skull bone, mosquito cuticle, wasp cuticle, and rat dura over a wide spectral range from 450 nm to 1624 nm at a spatial resolution of ~25 μm for ballistic transmission and ~50 μm for total transmission. These results will be valuable for MPM, where knowing the ballistic transmission, total transmission, and transmission heterogeneity of the sample are necessary to determine the optimal excitation wavelength and the fluorophores.

Disclosures. The authors declare that there are no conflicts of interested related to this article.

Data availability. Data presented in this paper are available in Dataset 1 [24] and Dataset 2 [25].

Supplemental document. See Supplement 1 for supporting content.

References

1. F. Xia, C. Wu, D. Sinefeld, B. Li, Y. Qin, and C. Xu, "In vivo label-free confocal imaging of the deep mouse brain with long-wavelength illumination," Biomed. Opt. Express **9**(12), 6545 (2018).
2. G. Hong, S. Diao, J. Chang, A. L. Antaris, C. Chen, B. Zhang, S. Zhao, D. N. Atochin, P. L. Huang, K. I. Andreasson, C. J. Kuo, and H. Dai, "Through-skull fluorescence imaging of the brain in a new near-infrared window," Nat. Photonics **8**(9), 723–730 (2014).
3. N. G. Horton, K. Wang, D. Kobat, C. G. Clark, F. W. Wise, C. B. Schaffer, and C. Xu, "In vivo three-photon microscopy of subcortical structures within an intact mouse brain," Nat. Photonics **7**(3), 205–209 (2013).
4. M. Wang, C. Wu, D. Sinefeld, B. Li, F. Xia, and C. Xu, "Comparing the effective attenuation lengths for long wavelength in vivo imaging of the mouse brain," Biomed. Opt. Express **9**(8), 3534 (2018).
5. F. Xia, M. Gevers, A. Fognini, A. T. Mok, B. Li, N. Akbari, I. E. Zadeh, J. Qin-dregely, and C. Xu, "Short-wave infrared confocal fluorescence imaging of deep mouse brain with a superconducting nanowire single-photon detector," ACS Photonics **8**(9), 2800–2810 (2021).
6. W. Denk, J. H. Strickler, and W. W. Webb, "Two-photon laser scanning fluorescence microscopy," Science **248**(4951), 73–76 (1990).
7. T. Wang, D. G. Ouzounov, C. Wu, N. G. Horton, B. Zhang, C. H. Wu, Y. Zhang, M. J. Schnitzer, and C. Xu, "Three-photon imaging of mouse brain structure and function through the intact skull," Nat. Methods **15**(10), 789–792 (2018).
8. T. Wang, C. Wu, D. G. Ouzounov, W. Gu, F. Xia, M. Kim, X. Yang, M. R. Warden, and C. Xu, "Quantitative analysis of 1300-nm three-photon calcium imaging in the mouse brain," Elife **9**, 1–22 (2020).
9. K. Podgorski and G. Ranganathan, "Brain heating induced by near-infrared lasers during multiphoton microscopy," J. Neurophysiol. **116**(3), 1012–1023 (2016).
10. M. Wang, M. Kim, F. Xia, and C. Xu, "Impact of the emission wavelengths on in vivo multiphoton imaging of mouse brains," Biomed. Opt. Express **10**(4), 1905 (2019).
11. C. Xu and W. W. Webb, "Measurement of two-photon excitation cross sections of molecular fluorophores with data from 690 to 1050 nm," J. Opt. Soc. Am. B **13**(3), 481 (1996).
12. X. Deng, Z. Zhuang, H. Liu, P. Qiu, and K. Wang, "Measurement of 3-photon excitation and emission spectra and verification of Kasha's rule for selected fluorescent proteins excited at the 1700-nm window," Opt. Express **27**(9), 12723 (2019).
13. C. P. Sabino, A. M. Deana, T. M. Yoshimura, D. F. T. Da Silva, C. M. França, M. R. Hamblin, and M. S. Ribeiro, "The optical properties of mouse skin in the visible and near infrared spectral regions," J. Photochem. Photobiol. B Biol. **160**, 72–78 (2016).
14. S. Golovynskyi, I. Golovynska, L. I. Stepanova, O. I. Datsenko, L. Liu, J. Qu, and T. Y. Ohulchanskyy, "Optical windows for head tissues in near-infrared and short-wave infrared regions: Approaching transcranial light applications," J. Biophotonics **11**(12), e201800141 (2018).
15. M. Azimipour, R. Baumgartner, Y. Liu, S. L. Jacques, K. Eliceiri, and R. Pashaie, "Extraction of optical properties and prediction of light distribution in rat brain tissue," J. Biomed. Opt. **19**(7), 075001 (2014).
16. D. J. Segeistein, "*The complex refractive index of water*," University of Missouri-Kansas City (1975).
17. H. Soleimanzad, H. Gurden, and F. Pain, "Optical properties of mice skull bone in the 455- to 705-nm range," J. Biomed. Opt. **22**(1), 010503 (2017).
18. E. A. Genina, A. N. Bashkatov, D. K. Tuchina, P. A. Dyachenko, N. Navolokin, A. Shirokov, A. Khorovodov, A. Terskov, M. Klimova, A. Mamedova, I. Blokhina, I. Agranovich, E. Zinchenko, O. V. Semyachkina-Glushkovskaya, and V. V. Tuchin, "Optical properties of brain tissues at the different stages of glioma development in rats: pilot study," Biomed. Opt. Express **10**(10), 5182 (2019).
19. C. Mätzler, *MATLAB Functions for Mie Scattering and Absorption* (2002), Vol. 2002–08.
20. S. L. Jacques, "Optical properties of biological tissues: A review," Phys. Med. Biol. **58**(14), 5007–5008 (2013).
21. D. G. Ouzounov, T. Wang, M. Wang, D. D. Feng, N. G. Horton, J. C. Cruz-Hernández, Y.-T. Cheng, J. Reimer, A. S. Tolias, N. Nishimura, and C. Xu, "In vivo three-photon imaging of activity of GCaMP6-labeled neurons deep in intact mouse brain," Nat. Methods **14**(4), 388–390 (2017).
22. A. Y. Shih, J. D. Driscoll, P. J. Drew, N. Nishimura, C. B. Schaffer, and D. Kleinfeld, "Two-photon microscopy as a tool to study blood flow and neurovascular coupling in the rodent brain," J. Cereb. Blood Flow Metab. **32**(7), 1277–1309 (2012).
23. D. Débarre, W. Supatto, A. M. Pena, A. Fabre, T. Tordjmann, L. Combettes, M. C. Schanne-Klein, and E. Beaurepaire, "Imaging lipid bodies in cells and tissues using third-harmonic generation microscopy," Nat. Methods **3**(1), 47–53 (2006).
24. A. Mok, "Data Set 1 for "Spatially resolved measurements of ballistic and total transmission in microscale tissue samples from 450 nm to 1624 nm," figshare, 2021, https://doi.org/10.6084/m9.figshare.16528887.
25. A. Mok, "Data Set 2 for "Spatially resolved measurements of ballistic and total transmission in microscale tissue samples from 450 nm to 1624 nm," figshare, 2021, https://doi.org/10.6084/m9.figshare.16528890.

26. M. Firbank, M. Hiraoka, M. Essenpreis, and D. T. Delpy, "Measurement of the optical properties of the skull in the wavelength range 650-950 nm," Phys. Med. Biol. **38**(4), 503–510 (1993).

27. A. N. Bashkatov, E. A. Genina, V. I. Kochubey, and V. V. Tuchin, "Optical properties of human cranial bone in the spectral range from 800 to 2000nm," in *Proceedings of SPIE* (2006), Vol. 6163, pp. 616310–11.

28. S. Rotter and S. Gigan, "Light fields in complex media: Mesoscopic scattering meets wave control," Rev. Mod. Phys. **89**(1), 015005 (2017).